CASTOR: A FORWARD DETECTOR FOR THE IDENTIFICATION OF CENTAURO AND STRANGELETS IN NUCLEUS–NUCLEUS COLLISIONS AT THE LHC *

A.L.S. ANGELIS[a], J. BARTKE[b], M.YU. BOGOLYUBSKY[c], S.N. FILIPPOV[d], E. GŁADYSZ-DZIADUŚ[b], YU.V. KHARLOV[c], A.B. KUREPIN[d], A.I. MAEVSKAYA[d], G. MAVROMANOLAKIS[a], A.D. PANAGIOTOU[a], S.A. SADOVSKY[c], P. STEFANSKI[b], Z. WŁODARCZYK[e]

[a] *Nuclear and Particle Physics Division, University of Athens, Hellas.*
[b] *Institute of Nuclear Physics, Cracow, Poland.*
[c] *Institute for High Energy Physics, Protvino, Russia.*
[d] *Institute for Nuclear Research, Moscow, Russia.*
[e] *Institute of Physics, Pedagogical University, Kielce, Poland.*

The physics motivation for a very forward detector to be employed in heavy ion collisions at the CERN LHC is discussed. A phenomenological model describing the formation and decay of a Centauro fireball in nucleus-nucleus collisions is presented. The CASTOR detector which is aimed to measure the hadronic and photonic content of an interaction and to identify deeply penetrating objects in the very forward, baryon-rich phase space $5.6 \leq \eta \leq 7.2$ in an event-by-event mode is described. Results of simulations of the expected response of the calorimeter, and in particular to the passage of strangelets, are presented.

1 Introduction

The ALICE detector [1], which is aimed at investigating nucleus–nucleus collisions at the LHC, will be fully instrumented for hadron and photon identification only in the limited angular region around mid-rapidity, covering the pseudorapidity interval $|\eta| \leq 1$. An additional muon detector [2] will be installed on one side and will cover the pseudorapidity interval $2.5 \leq \eta \leq 4.0$. A pre-shower photon multiplicity detector [3] will also be installed on one side and will cover the pseudorapidity interval $2.3 \leq \eta \leq 3.3$. Finally a small-aperture zero degree calorimeter is also foreseen, at a distance of about 100 m from the interaction point, to provide the centrality trigger. The very small acceptance and lack of longitudinal and transverse segmentation in the present design of the zero degree calorimeter make it suitable for this purpose only.

This constitutes only a small part of the total available phase space which, at the design beam energy of 2.75 A TeV for *Pb* ions at the LHC, extends to $|\eta| = 8.7$. Already at the early stages of the preparation of the ALICE proposal some of us pointed out that there is interesting physics beyond mid-rapidity [4,5]. From these considerations evolved the idea of a dedicated for-

*Presented at XXVIII Int. Symp. on Multiparticle Dynamics, 6-11 Sep. 1998, Delphi.
Further information at: http://home.cern.ch/~angelis/castor/Welcome.html

ward detector, CASTOR [6,7], to provide physics information on hadrons and photons emitted in the fragmentation region. At LHC *Pb*-ion energies this region of phase space extends beyond $|\eta| = 5$ or 6, depending on the effective baryonic stopping power which is different for the various Monte-Carlo models employed. In this region of extremely high baryon number density one can expect to discover new phenomena related to the high baryochemical potential, in particular the formation of Deconfined Quark Matter (DQM), which could exist e.g. in the core of neutron stars, with characteristics different from those expected in the much higher temperature baryon-free region around mid-rapidity,

The LHC, with an energy equivalent to 10^{17} eV for a moving proton impinging on one at rest, will be the first accelerator to effectively probe the highest cosmic ray energy domain. Cosmic ray experiments have detected numerous most unusual events whose nature is still not understood. These events, observed in the projectile fragmentation rapidity region, will be produced and studied at the LHC in controlled conditions. Here we mention the "Centauro" events and the "long-flying component". Centauros [8] exhibit relatively small multiplicity, complete absence (or strong suppression) of the electromagnetic component and very high $\langle p_{\mathrm{T}} \rangle$. In addition, some hadron-rich events are accompanied by a strongly penetrating component observed in the form of halo, strongly penetrating clusters [9,10] or long-living cascades, whose transition curves exhibit a characteristic form with many maxima [11,12].

2 A model for the production of Centauro and Strangelets

A model has been developed in which Centauros are considered to originate from the hadronization of a DQM fireball of very high baryon density ($\rho_{\mathrm{b}} \gtrsim 2$ fm^{-3}) and baryochemical potential ($\mu_{\mathrm{b}} >> \mathrm{m_n}$), produced in ultra-relativistic nucleus–nucleus collisions in the upper atmosphere [13,14,15]. In this model the DQM fireball initially consists of u, d quarks and gluons. The very high baryochemical potential prohibits the creation of $\mathrm{u\bar{u}}$ and $\mathrm{d\bar{d}}$ quark pairs because of Pauli blocking of u and d quarks and the factor exp $(-\mu_{\mathrm{q}}/\mathrm{T})$ for $\bar{\mathrm{u}}$ and $\bar{\mathrm{d}}$ antiquarks, resulting in the fragmentation of gluons into $\mathrm{s\bar{s}}$ pairs predominantly. In the subsequent hadronization this leads to the strong suppression of pions and hence of photons, but allows kaons to be emitted, carrying away strange antiquarks, positive charge, entropy and temperature. This process of strangeness distillation transforms the initial quark matter fireball into a slightly strange quark matter state. In the subsequent decay and hadronization of this state non-strange baryons and strangelets will be formed. Simulations show that strangelets could be identified as the strongly penetrating particles frequently seen accompanying hadron-rich cosmic ray events [5,16]. In this manner, both the basic characteristics of the Centauro events (small multiplicities and extreme imbalance of hadronic to photonic content) and the strongly penetrating component are naturally explained. In table 1 we compare characteristics of Centauro and strongly penetrating components (strangelets), either experimentally observed or calculated within the context of the above model, for cosmic ray interactions and for nucleus–nucleus interactions at the LHC.

Table 1. Average characteristic quantities of Centauro events and Strangelets produced in Cosmic Rays and expected at the LHC.

Centauro	Cosmic Rays	LHC
Interaction	"$Fe + N$"	$Pb + Pb$
$\sqrt{s}$	$\gtrsim$ 6.76 TeV	5.5 TeV
Fireball mass	$\gtrsim$ 180 GeV	$\sim$ 500 GeV
y_{proj}	≥ 11	8.67
γ	$\geq 10^4$	$\simeq 300$
η_{cent}	9.9	$\simeq 5.6$
$\Delta\eta_{cent}$	1	$\simeq 0.8$
$< p_T >$	1.75 GeV	1.75 GeV (*)
Life-time	10^{-9} s	10^{-9} s (*)
Decay prob.	10 % (x $\geq$ 10 km)	1 % (x $\leq$ 1 m)
Strangeness	14	60 - 80
f_s (S/A)	$\simeq 0.2$	0.30 - 0.45
Z/A	$\simeq 0.4$	$\simeq 0.3$
Event rate	$\gtrsim$ 1 %	$\simeq$ 1000/ALICE-year
"Strangelet"	Cosmic Rays	LHC
Mass	$\simeq$ 7 - 15 GeV	10 - 80 GeV
Z	$\lesssim 0$	$\lesssim 0$
f_s	$\simeq 1$	$\simeq 1$
η_{str}	$\eta_{cent} + 1.2$	$\eta_{cent} + 1.6$

(*) assumed

3 The design of the CASTOR detector

With the above considerations in mind we have designed the CASTOR (Centauro And STrange Object Research) detector, to be placed in the fragmentation region. CASTOR will cover the pseudorapidity interval $5.6 \leq \eta \leq 7.2$. Figures 1, 2, 3 and 4 depict the hadron and photon pseudorapidity distributions as predicted by the HIJING Monte-Carlo generator for central $Pb + Pb$

collisions at the LHC. The upper plots show distributions of multiplicity while the lower plots show distributions of energy flux. Figures 5 and 6 depict the baryon number pseudorapidity distributions as predicted by the HIJING and VENUS Monte-Carlo generators for central $Pb + Pb$ collisions at the LHC. The acceptance of CASTOR is superimposed on each plot. As can be seen from the plots, while CASTOR will receive a moderate multiplicity, its position has been optimized to probe the maximum of the baryon number density and energy flow and to identify any effects connected with these conditions.

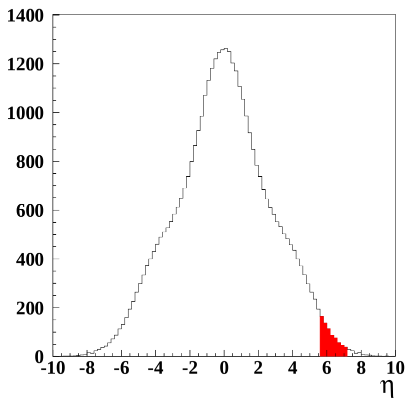

Figure 1. Average photon multiplicity pseudorapidity distribution obtained from 50 central $Pb + Pb$ HIJING events.

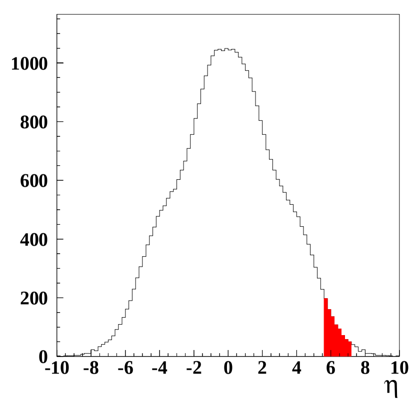

Figure 2. Average charged particle multiplicity pseudorapidity distribution obtained from 50 central $Pb + Pb$ HIJING events.

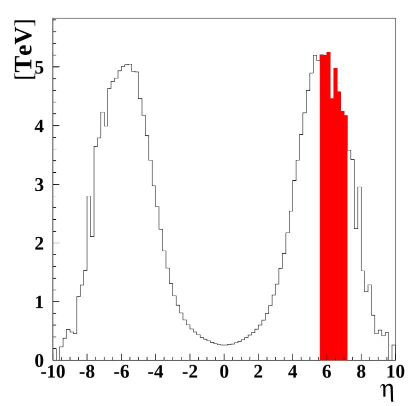

Figure 3. Average electromagnetic energy pseudorapidity distribution obtained from 50 central $Pb + Pb$ HIJING events.

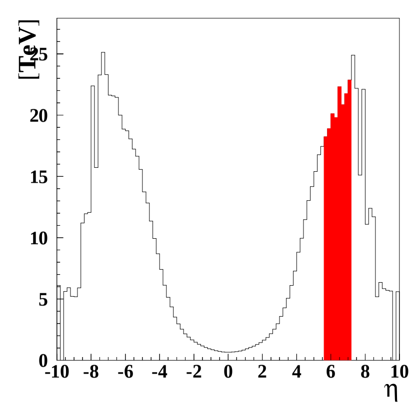

Figure 4. Average hadronic energy pseudorapidity distribution obtained from 50 central $Pb + Pb$ HIJING events.

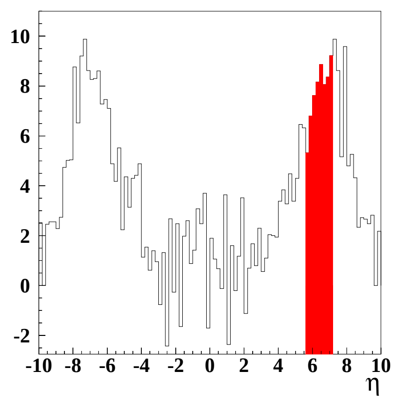

Figure 5. Average net baryon number pseudorapidity distribution obtained from 50 central $Pb + Pb$ HIJING events.

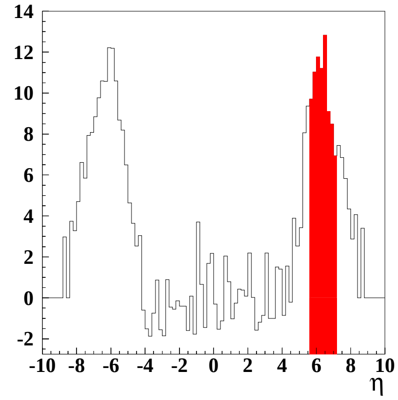

Figure 6. Average net baryon number pdeudorapidity distribution obtained from 47 central $Pb + Pb$ VENUS events.

A schematic view of the CASTOR detector [6,7] is shown in figure 7. It is optimized to measure the hadronic and photonic content of an interaction, both in energy and multiplicity, and to search for strongly penetrating particles. It will consist of a Si pad charged particle multiplicity detector followed by a Si pad pre-shower photon multiplicity detector and of a longitudinally segmented tungsten/quartz-fibre calorimeter with electromagnetic and hadronic sections.

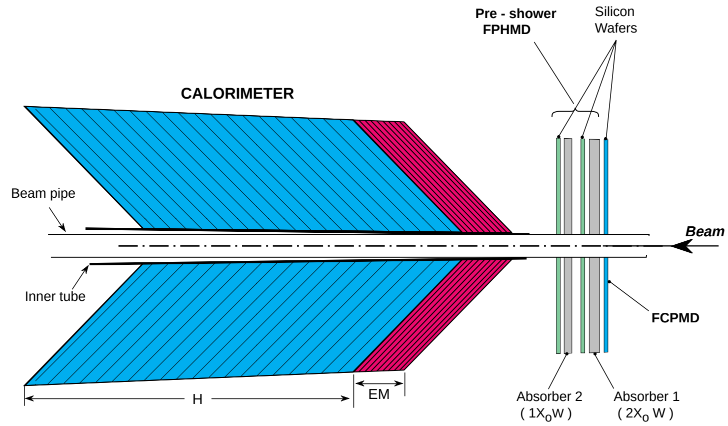

Figure 7. Schematic representation of the CASTOR detector.

The multiplicity detectors have the form of annular discs of about 129 mm outer and 26 mm inner radius, constructed in two half-rings to be positioned around the beam pipe.

The calorimeter is made of layers of active medium sandwiched between tungsten absorber plates. The active medium consists of planes of silica fibres and the signal is the Cherenkov light produced as they are traversed by the charged particles in the shower. The fibres are inclined at 45 degrees relative to the incoming particles to maximize light output. The calorimeter is azimuthally divided into 8 octants. Each octant is longitudinally segmented into 80 layers, the first 8 ($\simeq$ 14.7 X_0) comprising the electromagnetic section and the remaining 72 ($\simeq$ 9.47 λ_I) the hadronic section. The light output from groups of 4 consecutive active layers is coupled into the same light guide, giving a total of 20 readout channels along each octant. More detailed specifications are given in table 2 and a general view of the calorimeter, including its support, is shown in figure 8. Mechanically the calorimeter is a structure built in two sections, left and right, each consisting of four octants connected together at each corner through bolted plates. The two sections and each of the octants are self-supporting. It is envisaged to cut the edges of the absorber plates in the azimuthal direction at an angle in such a way as to avoid cracks between adjacent modules. The outer plates shown in figure 8 (one omitted for clarity) constitute the support for the light guides and photomultipliers.

Table 2. CASTOR calorimeter specifications.

	Electromagnetic	Hadronic
Material	Tungsten + Quartz Fibre	Tungsten + Quartz Fibre
Dimensions	$\langle R_{in} \rangle = 26$ mm,	$\langle R_{in} \rangle = 27$ mm,
	$\langle R_{out} \rangle = 129$ mm	$\langle R_{out} \rangle = 134$ mm
Absorber Plates	Thickness = 5 mm	Thickness = 10 mm
(at 45°)	Eff. thickness = 7.07 mm	Eff. thickness = 14.1 mm
No. Layers	8	72
Eff. length	56.6 mm $\simeq$ 14.7 $X_0 \simeq 0.53\ \lambda_I$	1018.1 mm $\simeq 9.47\ \lambda_I$
Quartz Fibre	$\sim$ 0.45 mm	$\sim$ 0.45 mm
No. QF planes	2 per sampling	4 per sampling
Sampling	$\simeq 1.84\ X_0$	$\simeq 0.13\ \lambda_I$
Reading	Coupling of 4 samplings	Coupling of 4 samplings
No. Readings	2	18
No. Channels	$2 \times 8 = 16$	$18 \times 8 = 144$
QF/W vol.	10%	10%

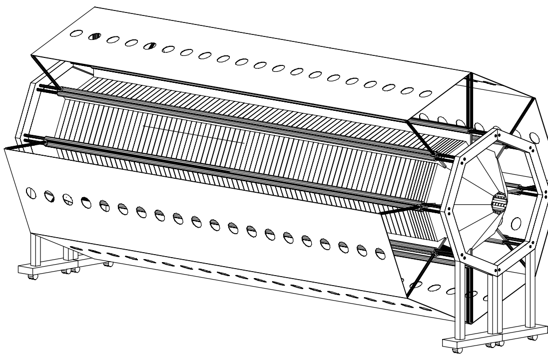

Figure 8. General view of the CASTOR calorimeter construction including support.

4 Simulation of the CASTOR calorimeter performance

We have made detailed GEANT simulations of the performance of the C A S T O R calorimeter. Figure 9 shows its response to one central $Pb + Pb$ HIJING event: figure 9a shows the number of charged particles (essentially e^+, e^-) above Cherenkov threshold in the showers at each active layer, while figure 9b shows the corresponding number of Cherenkov photons which are produced, captured and propagated inside the fibres.

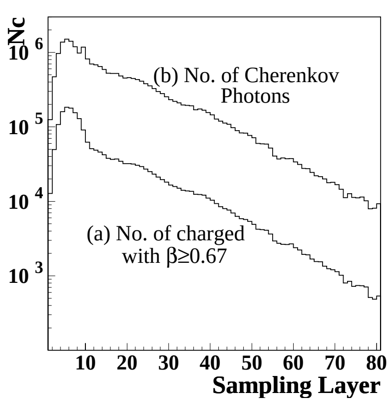

Figure 9. Response of the CASTOR calorimeter: (a) Number of charged particles above Cherenkov threshold at each active layer, (b) Number of Cherenkov photons produced and propagated inside the fibres at each active layer.

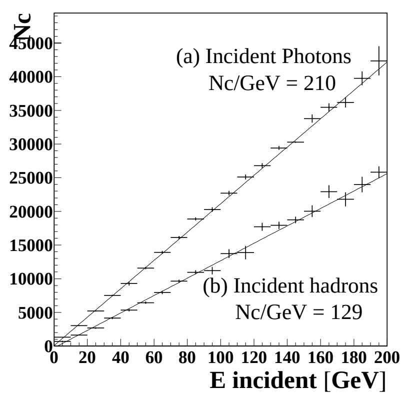

Figure 10. Total number of Cherenkov photons produced, captured and propagated inside the fibres, vs. incident particle energy: (a) For incident photons, (b) For incident hadrons.

Figure 10 shows the total number of Cherenkov photons produced, captured and propagated inside the fibres, as a function of the incident particle energy, for incident photons and hadrons from one central $Pb + Pb$ HIJING event. About 210 Cherenkov photons per GeV are obtained for incident photons and 129 Cherenkov photons per GeV for incident hadrons.

In addition we have simulated the interaction of a Strangelet with the calorimeter material, using the simplified picture described in [16,17]. As an example figure 11 shows the response of the calorimeter to one central $Pb + Pb$ HIJING event, which contains a Strangelet of A_{str}=20, E_{str}=20 TeV and quark chemical potential μ_{str}=600 MeV (energy conservation has been taken into account). Figure 11a shows the energy deposition along the octant containing the Strangelet, while figure 11b shows the average of the energy deposition along the other seven octants.

The study of such simulated events shows that the signal from an octant containing a Strangelet is larger than the average of the others, while its transition curve displays long penetration and many maxima structure, such as observed in cosmic ray events.

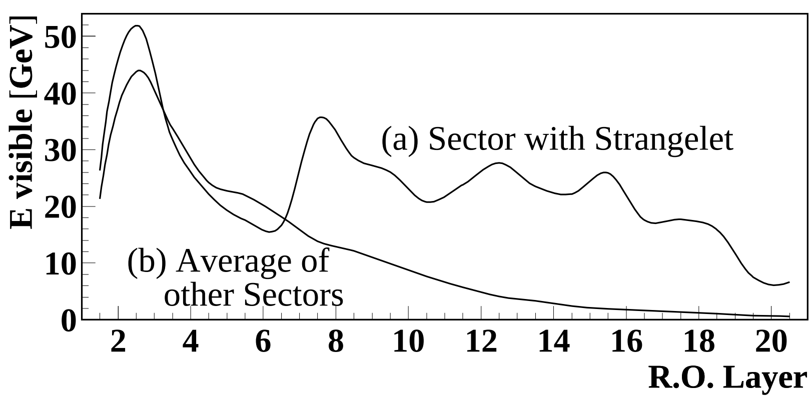

Figure 11. Energy deposition in the readout layers (couplings of 4 consecutive sampling layers) of the CASTOR calorimeter: (a) In the octant containing the Strangelet, (b) Average of the other octants.

5 Conclusions

We have designed a detector system well suited to probe the very forward region in $Pb+Pb$ collisions at the LHC, where very large baryon number density and energy flow occur. Our detector will identify any effects connected with these conditions. It has been particularly optimised to search for signatures of Centauro and for long penetrating objects. We have developed a model which explains Centauro production in cosmic rays and makes predictions for $Pb + Pb$ collisions at the LHC. Our model naturally incorporates the possibility of Strangelet formation. We have simulated the passage of Strangelets through the CASTOR calorimeter and we find long penetration and many-maxima structures similar to those observed in cosmic ray events.

Acknowledgements

This work has been partly supported by the Hellenic General Secretariat for Research and Technology ΠΕΝΕΔ 1361.1674/31-1/95, the Polish State Committee for Scientific Research grants 2P03B 121 12 and SPUB P03/016/97, and the Russian Foundation for Fundamental Research grant 96-02-18306.

References

1. The ALICE technical proposal, CERN/LHCC 95–71.
2. The ALICE forward muon spectrometer, CERN/LHCC 96–32.
3. Y.P. Viyogi, Note ALICE/PMD 98–52.
4. J. Bartke et al, Note ALICE/PHY 93–12.
5. E. Gładysz-Dziaduś and A.D. Panagiotou, Proc. Int. Symp. on Strangeness & Quark Matter, eds. G. Vassiliadis et al., World Scientific, 1995 p.265.
6. A.L.S. Angelis et al, CASTOR draft proposal, Note ALICE/CAS 97–07.
7. A.L.S. Angelis and A.D. Panagiotou, J. Phys. G: Nucl. Part. Phys. **23** (1997) 2069.
8. C.M.G. Lates, Y. Fugimito and S. Hasegawa, Phys. Rep. **65** (1980) 151.
9. L.T. Baradzei et al., Nucl. Phys. **B370** (1992) 365.
10. S. Hasegawa and M. Tamada, Nucl. Phys. **B474** (1996) 225.
11. Z. Buja et al., Proc. 17th ICRC, Paris 1981, Vol.11 p.104.
12. T. Arisawa et al., Nucl. Phys. **B424** (1994) 241.
13. A.D. Panagiotou et al., Z. Phys. **A333** (1989) 355.
14. A.D. Panagiotou, A. PEtridis, M. Vassiliou, Phys. Rev. **D45** (1992) 3134.
15. M.N. Asprouli, A.D. Panagiotou, E. Gładysz-Dziaduś, Astropart. Phys. **2** (1994) 167.
16. E. Gładysz-Dziaduś and Z. Włodarczyk, J. Phys. G: Nucl. Part. Phys. **23** (1997) 2057.
17. A.L.S. Angelis, J. Bartke, E. Gładysz-Dziaduś, Z. Włodarczyk, INP 1800/PH, Kraków 1998.